

We are IntechOpen, the world's leading publisher of Open Access books Built by scientists, for scientists

6,900

Open access books available

186,000

International authors and editors

200M

Downloads

Our authors are among the

154

Countries delivered to

TOP 1%

most cited scientists

12.2%

Contributors from top 500 universities



WEB OF SCIENCE™

Selection of our books indexed in the Book Citation Index
in Web of Science™ Core Collection (BKCI)

Interested in publishing with us?
Contact book.department@intechopen.com

Numbers displayed above are based on latest data collected.
For more information visit www.intechopen.com



Electrochemical Probe for Frictional Force and Bubble Measurements in Gas-Liquid-Solid Contactors and Innovative Electrochemical Reactors for Electrocoagulation/Electroflotation

Abdel Hafid Essadki

*Ecole Supérieure de Technologie de Casablanca, Oasis, Casablanca
Hassan II Aïn Chock University
Morocco*

1. Introduction

Electrochemistry constitutes an important discipline that involves many phenomena as mass transfer, migration because of the presence of electric field, and hydrodynamic especially in reactor with large scale.

In fact, electrochemical methods and electrochemical reactors have to be developed in order to resolve many problems in different area (mining, waste water treatment etc).

For measurement by electrochemical methods, probes have to be developed. For example, knowledge of the magnitude of the frictional forces between the solids and the gas-liquid mixture is very important for design of bioreactors. The growth of biomass on solid surfaces may be sensitive to shear stress. In fluidized bed bioreactors the suspended carriers are used for microbial immobilization or enzyme encapsulation. The knowledge of shear stress is important because some micro-organisms and cells attached to microcarriers are sensitive to excessive friction. The aim is to develop and verify a fast and inexpensive method for measuring the frictional forces in multiphase reactors beds.

On the other hand the performance of a multiphase reactor – for example, a bubble column- depends on the knowledge the bubble swarm properties as bubble shape, velocity allowing to determine the gas liquid mass transfer and liquid solid mass transfer.

To establish direct local information and precise bubble dimensions, various probes were used. The electrical resistivity probe was developed to measure the velocity and diameter of a bubble in a conducting liquid medium. In a non-conducting medium, the optical probe is more appropriate.

To ensure easy measurement of bubble sizes in a non transparent conducting medium and to establish direct local information in a reactor, the present work shows the possible use of electrochemical probe.

Paragraph two develops this aspect, the electrochemical probe developed serves in the same time as a probe able to measure the velocity gradient at the wall of a spherical sphere and to measure the volume bubble in a bubble column.

For the process aspect as the water and waste water treatment, the need of purifying water for human consumption is more and more required. Cleaning wastewater from industrial effluents before discharging is also a challenging work. In fact, innovative, cheap and effective techniques have to be developed.

Electrocoagulation (EC) is an electrochemical method for treating polluted water which has been successfully applied for treatment of soluble or colloidal pollutants, such as wastewater containing heavy metals, emulsions, suspensions, etc., but also drinking water for lead or fluoride removal. A typical EC unit includes therefore an EC cell/reactor, a separator for settling or flotation, and often a filtration step. Indeed, the benefits of EC include simplicity, efficiency, environmental compatibility, safety, selectivity, flexibility and cost effectiveness. In particular, the main points involve the reduction of sludge generation, the minimization of the addition of chemicals and little space requirements due to shorter residence time. The main deficiency is the lack of dominant reactor design and modeling procedures. The literature reveals any systematic approach for design and scale-up purpose. The most papers use laboratory-scale EC cells in which magnetic stirring is adjusted experimentally and the separation step by floatation/sedimentation is not studied.

That's why an innovative reactor is developed in order to optimize the cost of this process. This is the object of paragraph three.

2. Electrochemical method for measurements of frictional force and bubble size

This part involves the measurement character of electrochemical methods that lead to measure the velocity gradient and frictional force on a particle in a bubble column and in a fluidized bed. The possibility of measuring bubble volume is also discussed. Thus, an electrochemical probe may be proposed to measure in the same time the frictional force and the bubble volume. The application of such electrochemical method is very important in biochemical engineering.

2.1 Velocity gradient and frictional force measurement

Reiss and Hanratty (1963) developed a model to obtain the velocity gradient S_w , in the vicinity of a wall of rectangular or cylindrical shape. By using a microelectrode mounted flush with a tube wall, the apparent mass transfer coefficient K_a could be obtained by electrochemical technique. This model was established in the cases where the thickness of the concentration boundary layer (δ_c) was less than that of the hydrodynamic boundary layer (δ_v) (figure 1) and was verified in cases of high Schmidt number.

The mass balance in the vicinity of the microelectrode can be developed as follow:

$$\frac{\partial C}{\partial t} + S_w y \frac{\partial C}{\partial x} = D \frac{\partial^2 C}{\partial y^2} \quad (1)$$

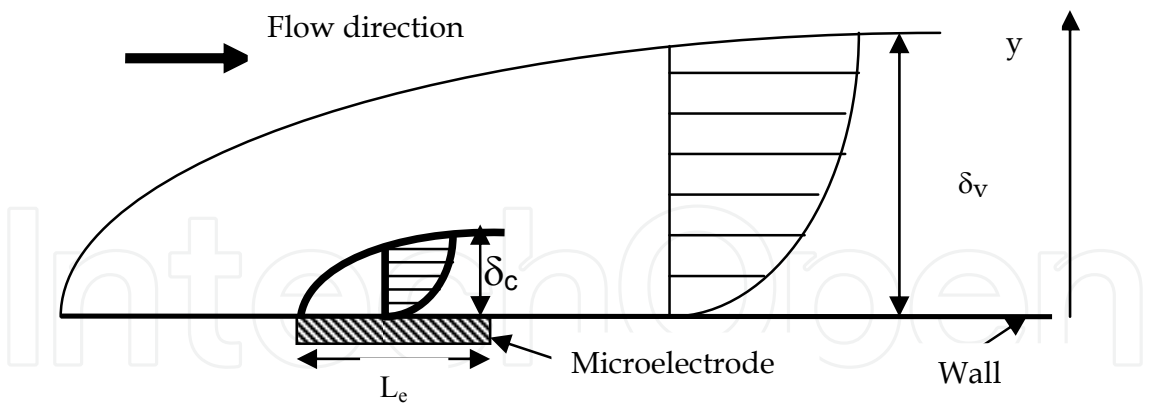


Fig. 1. Concentration and velocity profiles over the electrode surface.

The instantaneous rate of mass transfer is proportional to the concentration gradient at the surface averaged over the electrode:

$$N = D \left\langle \frac{\partial C}{\partial y} \right\rangle \tag{2}$$

The mass transfer coefficient defined as : $K_a = N / (C - C_w)$, C_w is the wall concentration.

The analytical solution of (1) allows to determine the local mass transfer coefficient::

$$\overline{K_a} = \alpha \left(\frac{D^2 S_w}{L_e} \right)^{1/3} \tag{3}$$

C : concentration, mol.m⁻³
D : coefficient diffusion, m².s⁻¹,

The method can be extended to spherical walls (sphere particle). A sphere is equipped with an inside channel, bent through 90°, in which a gold thread of 1 mm diameter was introduced, cut flush with the surface. A rigid tube serves as support. The microelectrode can be directed relative to the average direction of the liquid by rotating the support (figure 2).

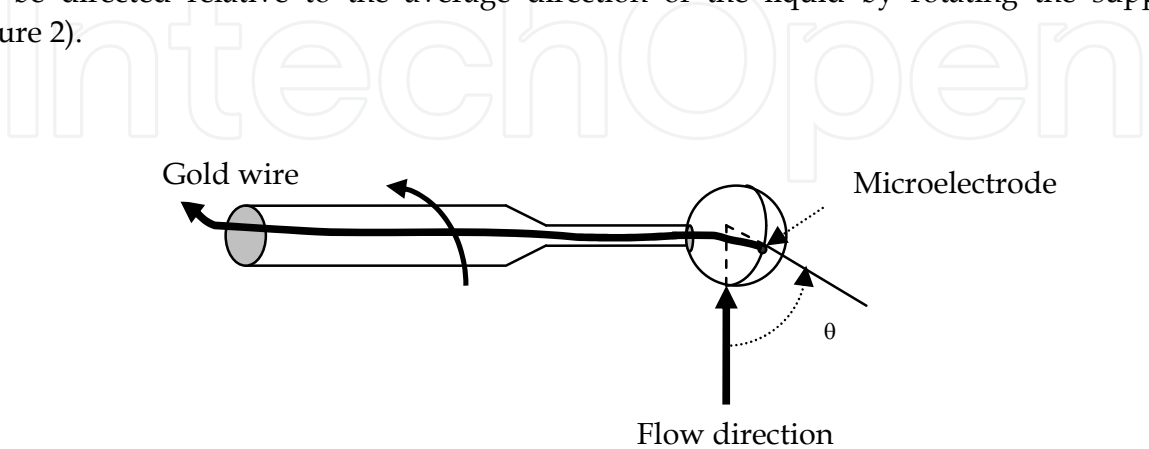


Fig. 2. The electrochemical electrode.

The electrochemical technique adopted consisted of the determination of the apparent local transfer coefficient (and subsequently the velocity gradient at the wall), based on measurements of the diffusion – limiting current during the reduction of an electroactive species.

The relationship between the apparent mass transfer coefficient and the velocity gradient is then deduced:

$$\overline{K_a} = 0.862 \left(\frac{D^2 \overline{S_w}}{d_e} \right)^{1/3} \quad (4)$$

d_e : diameter of microelectrode, m

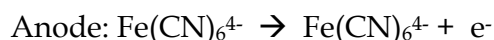
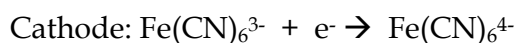
In order to test the validity of this model to predict the frictional force in sphere particles in bubble column and fluidized bed, the experimental apparatus is then designed (figure 3).

It is composed of a plexiglass fluidization column, 157 cm height (distance between the perforated stainless steel plate serving as liquid distributor and the point of liquid overflow) and 9.4 cm diameter. A column filled with glass sphere was placed underneath the liquid distributor; this serves as a homogenization section to avoid any preferential passage phenomena. A liquid reservoir is equipped with a temperature controller and a liquid cooling coil. Rotameters are used to measure the flow rates of liquid and gas (nitrogen) which are introduced via a gas injector consisting of two concentric circular tubes with 90 regularly spaced holes (0.4 mm diameter). An auxiliary electrode (nickel ring), a reference electrode furnished with a Luggin's capillary and a working electrode are connected to a potentiometer which is linked to microcomputer performing the acquisition of electric current signals and computations of the average and fluctuating current intensities.

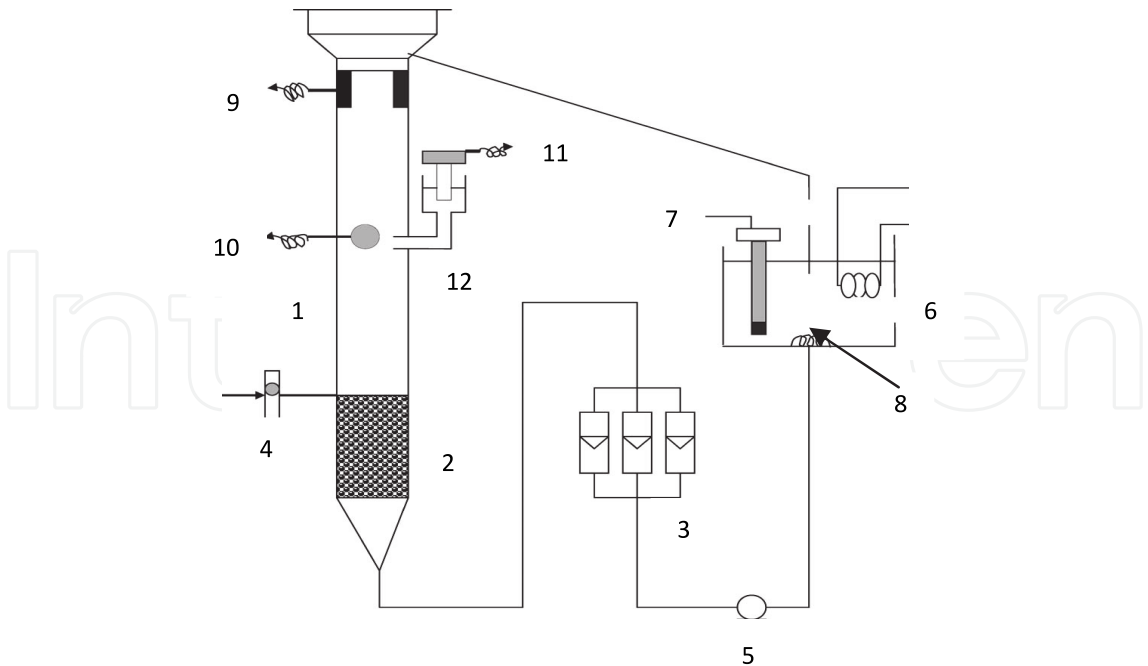
The method depends on creating a diffusional limitation at the transfer surface studied (working electrode) and simultaneously avoids such limitations at the counter electrode surface (i.e the counter electrode potential remained almost constant). This is achieved by using a counter electrode with a large surface area compared with the working electrode.

The intensity of the limiting current of the working electrode is obtained by the graph presenting the current intensity versus potential. In order to achieve this, the reference electrode (saturated calomel), has to be placed as closed as possible to the working electrode, to minimize the ohmic resistance of the solution. For this purpose, a capillary of about 1 mm diameter is introduced between the working and reference electrodes.

Several possible reactions for electrochemical determination of mass transfer coefficients are available, but the most frequently used system is potassium ferricyanide to potassium ferrocyanide. Normally the reaction at the working electrode is the reduction of ferricyanide, whereas the oxidation of ferrocyanide takes place at the counter electrode:



The ferricyanide concentration should thus in principle remain constant during the experiment. This is verified by using a turning disc electrode, as explained later. The



- | | |
|---------------------------|---------------------------|
| 1- Column | 7- Temperature controller |
| 2- Homogenization section | 8- Cooling coil |
| 3- Rotameter | 9- Auxiliary electrode |
| 4- Rotameters | 10- Working electrode |
| 5- Pump | 11- Reference electrode |
| 6- Liquid reservoir | 12- Capillary |

Fig. 3. Experimental apparatus for the study of friction on a solid sphere.

potassium ferri-ferrocyanide system chosen consisted of a 0.5 mol.dm⁻³ sodium hydroxide solution with 5 × 10⁻³ mol.dm⁻³ each of potassium ferricyanide and potassium ferrocyanide. Sodium hydroxide is added as electrolyte support to minimize the migrational effects.

The physic-chemical properties of the solution are given in Table 1. The density of the solution was determined by pycnometry and the viscosity measured by a viscosimeter (Rheomat 15T-FC). The diffusion coefficient of the potassium ferricyanide is measured by means of a turning disc electrode, computed from the intensity of the limiting current on the disc using the relationship (Levart & Schumann, 1974):

$$J = D C_0 Sc^{1/3} . (\omega / \nu)^{1/2} . 1/k \tag{5}$$

$$k = 1.61173 + 0.480306 Sc^{-1/3} + 0.23393 Sc^{-2/3} + 0.113151 Sc^{-1}$$

- D: coefficient diffusion, m².s⁻¹
J : molar flux species, mol.m⁻² s⁻¹
C₀ : electroactive species concentration, mol.m⁻³
ω : angular velocity, rd.s⁻¹
ν : kinematic velocity of liquid, m².s⁻¹
Sc : Schmidt number defined by ν/D

This relationship is also used to determine the concentration of the solution once the diffusion coefficient is known (assumed to be concentration independent).

Temperature (°C)	$10^{-3} \rho_l$ (kg.m ⁻³)	$10^3 \eta_l$ (Pa.s)	$10^{10} D$ (m ² .s ⁻¹)
25	1.02	1.17	5.17

Table 1. Physico-chemical properties of the solution used in the study.

The apparent mass transfer coefficient at any microelectrode position θ , is given by:

$$K_a = \frac{I_l}{n.F.A_e.C_0}$$

(6)

I_l : Intensity of diffusion – limiting current (A)
 F : Faraday constant (A s m⁻¹)
 n : number of electrons liberated during the course of the electrochemical reaction
 A_e :surface of microelectrode (m²).

From the equation (4) we can deduce the velocity gradient:

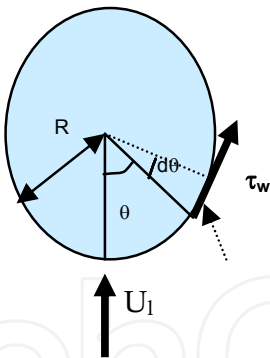
$$S_w(\theta) = (1.16K_a)^3 \cdot \frac{d_e}{D^2}$$

(7)

As the velocity gradient at the wall is related to the local shear stress (τ_w) through the relationship: $\tau_w = \eta_l \cdot S_w$ (Newtonian liquid), η_l is the dynamic viscosity (Pa.s).
Eq. (7) may be used to compute the frictional drag force (F_f) exerted on the whole sphere:

$$F_f = 2\pi R^2 \eta_l \int_0^\pi S_w(\theta) \sin^2\theta d\theta$$

(8)



Method verification:

The relationship of Reiss and Hanratty was established for the case of a flat surface and validity for a spherical surface should therefore first be verified.

Figure 4 shows the velocity gradient at the wall for five values of the Reynolds number and with different angles between the electrode surface and the mean fluid flow direction. The curves clearly show a maximum in velocity gradients around the 45° angle which is in agreement with calculations based on numerical solution of the momentum balance equation around a sphere. The figure also shows that the velocity gradient rises with the Reynolds number at all positions on the sphere. The influence is however far more noticeable in the front than in the rear of the sphere.

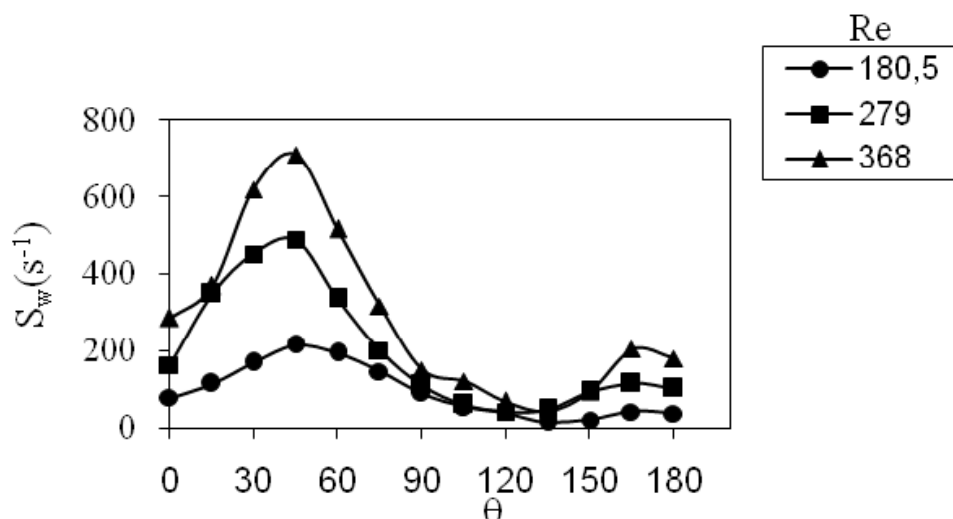


Fig. 4. Surface velocity gradient as function of position for single-phase around a sphere.

In the case of three phase fluidization, glass spheres (2mm in diameter, $\rho_s = 2532 \text{ kgm}^{-3}$) and plastic spheres (5mm in diameter, $\rho_s = 1388 \text{ kg.m}^{-3}$) are used. This choice provides very different bubbly flows due to different balances of coalescence and break-up of bubbles.

The contribution of the frictional force is more important in “coalescent” fluidized beds than in “break-up” fluidized beds. The effect of gas injection is depending on the fluidized particle effect on bubble coalescence and break-up. Correlations are developed linking frictional force to gas hold-up. The correlations recommended for frictional force in fluidized beds for both systems, (i.e., coalescence and break-up) are as follows:

- Glass spheres (2mm diameter, coalescence regime):
 $F = 2.43 \text{ Re}^{0.052} \varepsilon_g^{0.4}$, standard deviation = 6%.
- Plastic spheres (5mm diameter, break-up regime):
 $F = 0.123 \text{ Re}^{0.3} \varepsilon_g^{0.1}$, standard deviation = 4%.

F is a dimensionless force defined by $F = F_f/P_a$, where P_a is the effective weight of the sphere.

Re: Reynolds number defined by $d_p U_l \rho_l / \eta_l$, d_p is the particle diameter, ρ_l is the liquid density, U_l is the superficial liquid velocity, η_l is the dynamic viscosity, ε_g : gas holdup.

2.2 Bubble size measurement

The purpose is to demonstrate that the electrochemical probe can be used as a means of measuring bubble sizes. First, calibrated bubbles are used by single tubes. Then, a gas injector is used in a bubble column with homogeneous bubbling regime. In this case, the average frequency of the fluctuations of diffusion limited current detected by the probe is postulated as being equal to the bubble frequency leading to an estimation of bubble size.

2.2.1 Single orifice: bubble train

To test the possibility of measuring bubble size with the use of an electrochemical probe in a bubble column, a train of calibrated bubbles is generated in a tube in which gas is injected under closely controlled conditions. To obtain different bubble sizes, three tubes, T_1 , T_2 , and

T₄, with inner diameters of 1, 2, and 4 mm, respectively, are placed 5 cm below the probe. The probe is placed 30 cm above the liquid distributor and in the column center.

At low gas volumetric flow rates, the effect of the regular passage of bubbles close to the electrochemical probe on the diffusion limit current (or the velocity gradient) is studied. The stability of the bubble frequency is shown on the signal by regularly spaced peaks (fig.5). Signals similar to this are obtained for all positions of the front of the spherical probe (active surface) exposed to bubbles (0° < θ < 120°). The frequency spectrum clearly shows a single peak representing the bubble frequency, f_b (fig.6).

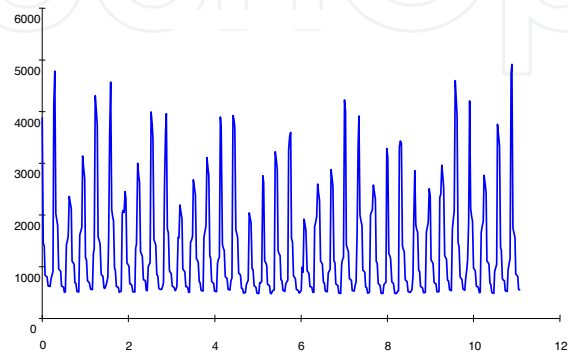


Fig. 5. History records of the velocity gradient at the wall: Effect of the regular passage of bubbles near the electrochemical probe.

Knowing the volumetric flow rate, Q_g, we can obtain the bubble volume, V_b by the relation:

$$V_b = \frac{Q_g}{f_b}$$

(9)

Assuming spherical bubbles, we can deduce the bubble diameter: d_b = (6V_b/π)^{1/3}.

A comparison at low gas flow rates is achieved by video recording when the bubble emission frequency and volume are obtained. Excellent agreement is observed, proving that the two methods give exactly the same frequency and the same average bubble diameter within 3%.

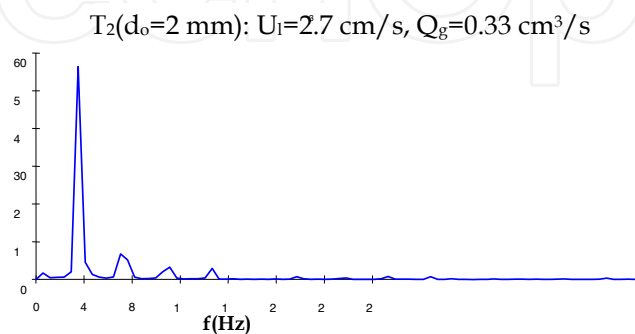


Fig. 6. Power spectral density function (P_s/s²): Effect of the regular passage of bubbles near the electrochemical probe.

2.2.2 Gas injector

In the case of a gas injector consisting of two concentric circular tubes with regularly spaced holes, the average frequency is used ($\langle f \rangle$) to evaluate the bubble diameter in the bubble column for the homogeneous bubbly flow. The bubble diameter is estimated by the following expression (Essadki et al., 1997):

$$d_b = 1.5 \frac{U_g}{\langle f \rangle} \quad (10)$$

The possibility of measuring bubble size by electrochemical probe is possible for the homogeneous bubbling regime in any conducting medium.

3. Innovative electrochemical reactors

This part describes the electrocoagulation and electroflotation as electrochemical methods to treat waste water. The conventional reactors used and the different disposition of electrodes are pointed out. It is also explained how innovative reactors can improve the process of waste water treatment. Thus, specific energy and electrode consumptions are even smaller without the need for mechanical agitation, pumping requirements and air injection, which could not be achieved in other kinds of conventional gas-liquid contacting devices.

An application is then presented to show the efficiency of electrocoagulation/electroflotation in removing colour from synthetic and real textile wastewater by using aluminum and iron electrodes in an external-loop airlift reactor. The defluoridation is also showed. The time, pH, conductivity and current density are the most parameters for the removal efficiency and energy consumption.

According to many authors, electrochemical technique such as electrocoagulation, electroflotation, electrodecantation have a lot of advantages comparatively to other techniques. Biological treatments are cheaper than other methods, but for example for the decolorization of dye wastewater, dye toxicity usually inhibits bacterial growth and limits therefore the efficiency of the decolorization. Physico-chemical methods include adsorption (e.g. on active carbon), coagulation-flocculation (using inorganic salts or polymers), chemical oxidation (chlorination, ozonisation, etc.) and photodegradation (UV/H₂O₂, UV/TiO₂, etc.). However, these technologies usually need additional chemicals which sometimes produce a secondary pollution and a huge volume of sludge. Water treatments based on the electrocoagulation technique have been recently proved to circumvent most of these problems, while being also economically attractive.

3.1 Electrocoagulation-electroflotation theories

This technique is based on the in situ formation of coagulant as the sacrificial anode (usually aluminum or iron) corrodes due to an applied current (figure 7). Aluminum and iron materials are usually used as anodes, the dissolution of which produces hydroxides, oxyhydroxides and polymeric hydroxides. In EC, settling is the most common option, while flotation may be achieved by H₂ (electroflotation) or assisted by air injection.

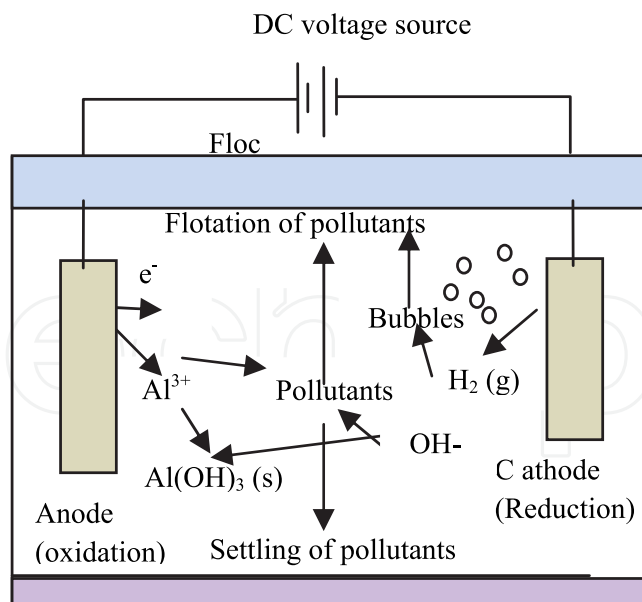


Fig. 7. Schematic diagram of two-electrode electrocoagulation (EC) cell.

Three successive stages occur during EC:

- i. Formation of coagulants by electrolytic oxidation of sacrificial anode
- ii. Destabilization of the pollutants, particulate suspension and breaking of emulsions
- iii. Aggregation of the destabilized phases to form flocs.

The pollutants can be in form of:

- Large particles easy to separate them from water by settling.
- Colloids.
- Dissolved mineral salt and organic molecules.

It is impossible to use the decantation as a technique to eliminate the maximum of particles. This remark is especially valid for colloids. Thus, colloids are organic or mineral particles in which the size is between some nanometers and approximately $1\ \mu$ responsible for color and turbidity.

The destabilization mechanism of the pollutants can be summarized as follows:

- Compression of the diffusion double layer around the charged species by the interactions of ions generated by oxidation of the sacrificial anode.
- Charge neutralization of the ionic species present in wastewater by counter ions produced by the electrochemical dissolution of the sacrificial anode. These counter ions reduce the electrostatic inter-particle repulsion to the extent that the Van Der Waals attraction predominates, thus causing coagulation. A zero net charge results in the process.
- Floc formation; the floc formed as a result of coagulation creates a sludge blanket that entraps and bridges colloidal particles still remaining in the aqueous medium.

3.2 Reactions at electrodes and different modes of electrodes connection

In the case of aluminum electrodes, the reactions taking place at the electrodes are as follow:

At the anode, takes place oxidation:



For higher current density:



At the cathode, takes place reduction:

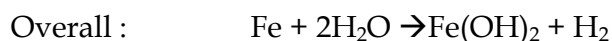
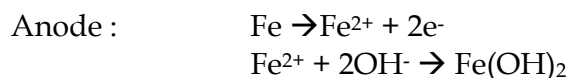


Although the sacrificial anodes deliver Al cation, their dissolution produces hydroxides, oxyhydroxides or polymeric hydroxides as a function of pH (Chen et al., 2004). These can adsorb or precipitate.

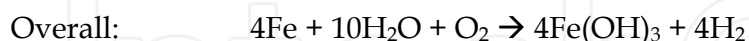
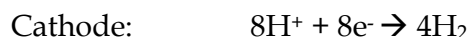
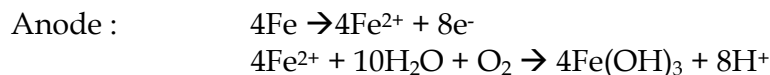
Al^{3+} ions may generate $\text{Al}(\text{H}_2\text{O})_6^{3+}$, $\text{Al}(\text{H}_2\text{O})_5\text{OH}^{2+}$, $\text{Al}(\text{H}_2\text{O})_4(\text{OH})^{2+}$. Many monomeric and polymeric species will be formed by hydrolysis such as, $\text{Al}(\text{OH})^{2+}$, $\text{Al}(\text{OH})_2^{+}$, $\text{Al}_2(\text{OH})_2^{4+}$, $\text{Al}(\text{OH})_4^{+}$, $\text{Al}_6(\text{OH})_{15}^{3+}$, $\text{Al}_7(\text{OH})_{17}^{4+}$, $\text{Al}_8(\text{OH})_{20}^{4+}$, $\text{Al}_{13}\text{O}_4(\text{OH})_{24}^{7+}$, $\text{Al}_{13}(\text{OH})_{34}^{5+}$ over a wide pH range.

In the case of iron electrodes, $\text{Fe}(\text{OH})_n$ with $n = 2$ or 3 is formed at the anode. The production of $\text{Fe}(\text{OH})_n$ follow two mechanisms.

a. Mechanism 1:



b. Mechanism 2:



Polymeric hydroxy complexes are also generated namely : $\text{Fe}(\text{H}_2\text{O})_6^{3+}$, $\text{Fe}(\text{H}_2\text{O})_5(\text{OH})^{2+}$, $\text{Fe}_2(\text{H}_2\text{O})_8(\text{OH})_{24}^{+}$ and $\text{Fe}_2(\text{H}_2\text{O})_6(\text{OH})_4^{4+}$, depending on the pH of aqueous medium.

Because of the workable rate of metal dissolution, a two-electrode EC is not always suitable. That's why large surface area is needed for a good performance. The electrodes configuration can be divided into three modes:

- Monopolar electrodes in parallel connections :

As observed in figure 8, the parallel arrangement consists of pairs of conductive metals plates placed between two parallel electrodes and DC power source. All cathodes are connected to each other and to negative pole of DC; in the same manner, all sacrificial anodes are connected to each other and to positive pole of DC. The electric current is divided between all the electrodes in relation to the resistance of the individual cells.

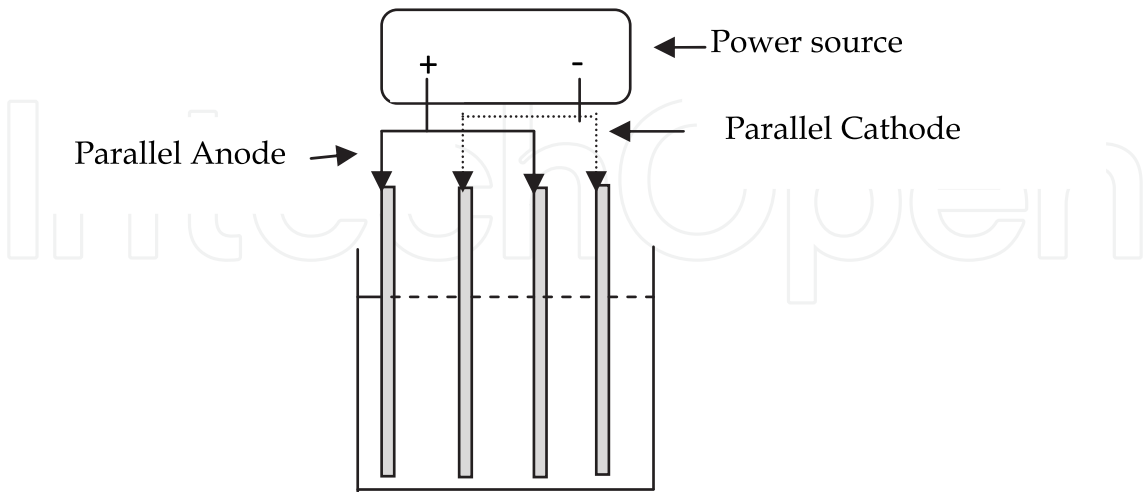


Fig. 8. Monopolar electrodes in parallel connections.

- Monopolar electrodes in series connections :

Each pair of sacrificial electrodes is internally connected with each other, and has no inter-connections with the outer electrodes (figure 9). The same current would flow through all the electrodes.

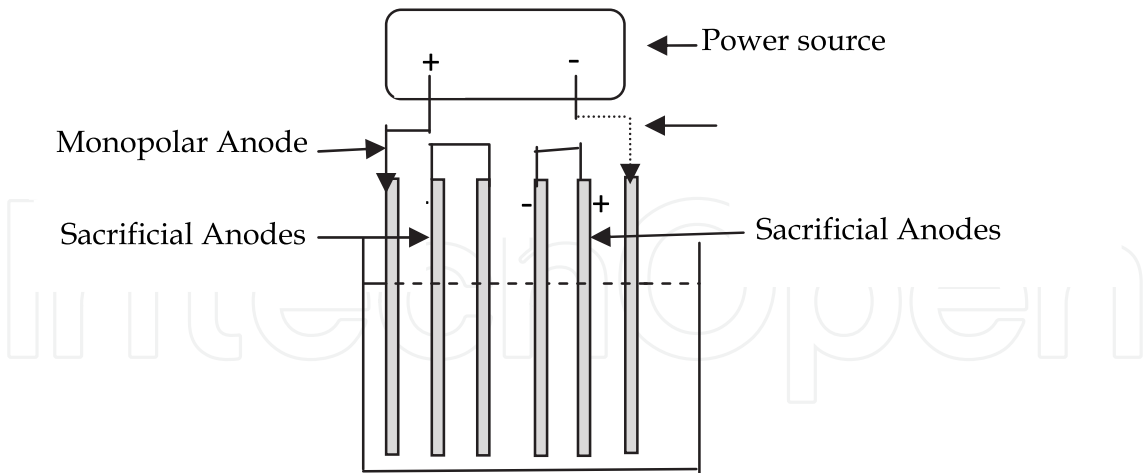


Fig. 9. Monopolar electrodes in series connections.

- Bipolar electrodes

The cells are in series. The sacrificial electrodes are placed between the two parallel electrodes without any electrical connection. Only the two monopolar electrodes are connected to the electric power source with no interconnections between the sacrificial electrodes.

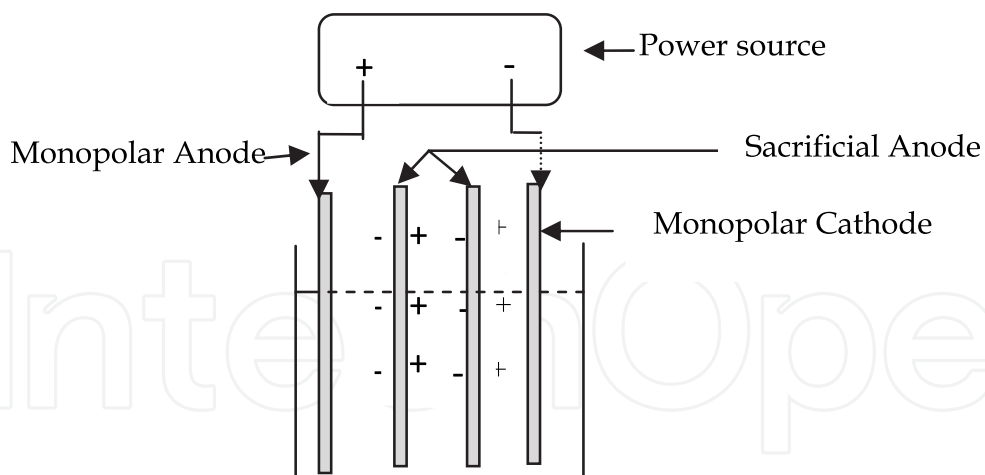


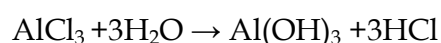
Fig. 10. Bipolar electrodes in series connections.

3.3 Parameters affecting electrocoagulation/electroflotation

Several parameters can affect the efficiency of removal by electrocoagulation/electroflotation. The most important parameters are described below.

3.3.1 Current density or charge loading

The current density (j) is expected to exhibit a strong effect on EC: higher the current, shorter the treatment. This is ascribed to the fact that at high current density, the extent of anodic dissolution of aluminum (iron) increases, resulting in a greater amount of precipitate for the removal of pollutants. Moreover, bubble generation rate increases and the bubble size decreases with increasing current density. These effects are both beneficial for high pollutant removal by H_2 flotation. As a first approximation, the amount of Al released is proportional to the product $\varphi_{Al}It$. The values of the Faradic yield φ_{Al} are between 100% and 160%; they decrease with increasing time in the first minutes of the run, but also with higher current density. These trends have already been reported in the literature (Essadki et al., 2009). This mass overconsumption of aluminum electrodes may be due to the chemical hydrolysis of the cathode but it also often explained by the “corrosion pitting” phenomenon which causes holes on the electrode surface. The mechanism suggested for “corrosion pitting” involves chloride anions and can be summarized as follows:



This mechanism can therefore produce more aluminum hydroxide flocs and H_2 bubbles than the equivalent current supplied should. Conversely, high current density allows the passivation of the cathode to be reduced but an increase in energy consumption that induces heating by Joule effect. As a result, too high current densities have generally to be avoided.

The specific electrode consumption per kg pollutant (μ_{Al}) is determined by the following expression:

$$\mu_{Al}(\text{kg Al} / \text{kg pollutant}) = \frac{3600 \cdot M_{Al} \cdot I \cdot t \cdot \phi_{Al}}{3F} \cdot \frac{1}{V(C_0 Y)} \quad (11)$$

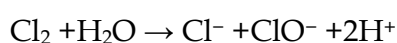
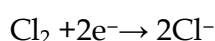
using initial pollutant concentration C_0 (kg/m³), current intensity I (A), cell voltage U (V), electrolysis time t (h), liquid volume V (m³), molar weight of aluminum $M_{Al} = 0.02698$ constant F (96,487 C/mole⁻) and the faradic yield ϕ_{Al} of Al dissolution, Y is the removal efficiency. ϕ_{Al} is estimated as the ratio of the weight loss of the aluminum electrodes during the experiments Δm_{exp} and the amount of aluminum consumed theoretically at the anode Δm_{th} :

$$\phi_{Al} = \frac{3F}{3600 \cdot M_{Al} \cdot I \cdot t} \cdot \Delta m_{exp} \quad (12)$$

This parameter depends upon the pH and the amount of other species present in solution, for example co-existing anions.

3.3.2 Conductivity

The increase of the conductivity (κ) by the addition of sodium chloride is known to reduce the cell voltage U at constant current density due to the decrease of the ohmic resistance of wastewater. Energy consumption, which is proportional to $U \cdot I$, will therefore decrease. Chloride ions could significantly reduce the adverse effects of other anions, such as HCO_3^- and SO_4^{2-} , for instance by avoiding the precipitation of calcium carbonate in hard water that could form an insulating layer on the surface of the electrodes and increase the ohmic resistance of the electrochemical cell (Chen et al., 2004). Chloride anions can also be oxidized and give active chlorine forms, such as hypochlorite anions, that can oxidize pollutants. The main mechanism is as follows:

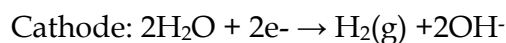
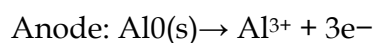


However, an excessive amount of NaCl (higher than 3 g/L) induces overconsumption of the aluminum electrodes due to “corrosion pitting” described above; Al dissolution may become irregular.

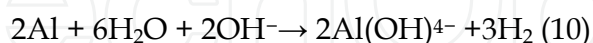
3.3.3 pH effect

pH is known to play a key role on the performance of EC. An optimum has to be found for the initial pH, in order to optimize the EC process. However, the pH changed during batch EC. Its evolution depended on the initial pH. EC process exhibits some buffering capacity because of the balance between the production and the consumption of OH^- (Chen et al., 2004), which prevents high change in pH. The buffering pH seems just above 7: when the initial pH is above this value, pH decreases during EC; otherwise, the opposite behavior is observed.

The effect of pH can be explained as follows. The main reactions during EC are:



At low pH, such as 2–3, cationic monomeric species Al^{3+} and $\text{Al}(\text{OH})^{2+}$ predominate. When pH is between 4–9, the Al^{3+} and OH^- ions generated by the electrodes react to form various monomeric species such as $\text{Al}(\text{OH})^{2+}$, $\text{Al}_2(\text{OH})_2^{2+}$, and polymeric species such as $\text{Al}_6(\text{OH})_{15}^{3+}$, $\text{Al}_7(\text{OH})_{17}^{4+}$, $\text{Al}_{13}(\text{OH})_{34}^{5+}$ that finally transform into insoluble amorphous $\text{Al}(\text{OH})_3(\text{s})$ through complex polymerization/precipitation kinetics. When pH is higher than 10, the monomeric $\text{Al}(\text{OH})_4^-$ anion concentration increases at the expense of $\text{Al}(\text{OH})_3(\text{s})$. In addition, the cathode may be chemically attacked by OH^- ions generated together with H_2 at high pH values:



Two main mechanisms are generally considered: *precipitation* for pH lower than 4 and adsorption for higher pH. Adsorption may proceed on $\text{Al}(\text{OH})_3$ or on the monomeric $\text{Al}(\text{OH})_4^-$.

3.3.4 Power supply

From an energetic point of view, energy consumption during EC is known to vary as the product UIt . Energy requirements per kg of pollutant removed ($E_{\text{pollutant}}$) to achieve a certain percentage of efficiency (Y) shows a continuous increase of $E_{\text{pollutant}}$ with j .

The specific electrical energy consumption per kg pollutant removed ($E_{\text{pollutant}}$) is calculated as follows:

$$E \text{ (kWh / kg pollutant)} = \frac{U.I.t.}{1000.V.(C_0 Y)} \quad (13)$$

3.3.5 Temperature

Few papers were investigated to show the effect of temperature on EC efficiency. The current efficiency of aluminum was found to be increased with temperature until about 60°C (Chen, 2004) where a maximum was found. Further increase in temperature results in a decrease of EC efficiency. The increase of temperature allows to a destruction of the aluminum oxide film on the electrode surface.

3.4 Design of electrocoagulation cell

The position of the electrodes in the reactor can be optimized as a function of hydrodynamic parameters and current density (j). Complementary rules should include the influences of electrode gap (e) and operating conditions on voltage U (and consequently on energy consumption). The measured potential is the sum of three contributions, namely the kinetic overpotential, the mass transfer overpotential and the overpotential caused by solution ohmic resistance. Kinetic and mass transfer overpotentials increase with current density, but mass transfer is mainly related to mixing conditions: if mixing is rapid enough, mass transfer overpotential should be negligible. In this case, the model described by Chen et al., (2004) is often recommended for non-passivated electrodes:

$$U = -0.76 + \frac{e}{k} j + 0.20 \ln(j) \quad (14)$$

Different typical reactors applied for electrochemical technologies are explained by Chen (2004).

3.5 Airlift reactors as innovative electrocoagulation cells

Airlift reactors constitute a particular class of bubble columns in which the difference in gas hold-up between two sections (namely, the riser and the downcomer) induces an overall liquid circulation without mechanical agitation (Chisti, 1989). They have been extensively applied in the process industry to carry out chemical and biochemical slow reactions, such as chemical oxidation using O_2 , Cl_2 or aerobic fermentation, but never as EC cells, as far as we know. Airlift reactors present two main designs: external-loop and internal-loop configurations (figure 11 a -b).

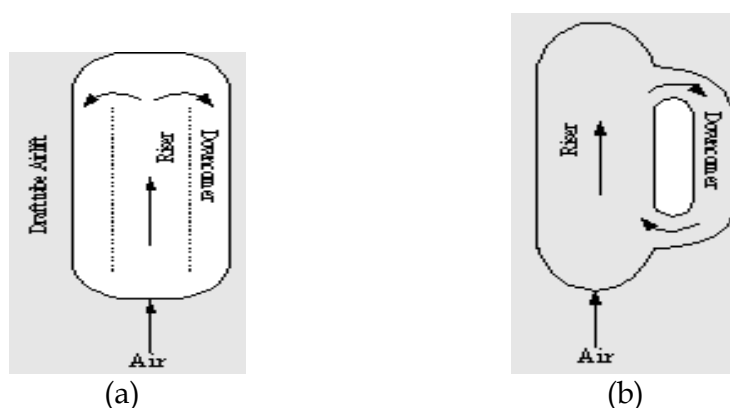


Fig. 11. Airlift reactors, (a) : internal loop airlift reactor, (b) : external loop airlift reactor.

External-loop airlift reactors offer the advantage to allow various designs of the separator section, which favors gas disengagement at the top of the reactor and maximizes consequently the overall recirculation velocity at the expense of more complex reactor geometries. Their hydrodynamics has also been extensively studied in two-phase gas-liquid and three-phase gas-liquid-solid flows. In airlift reactors, the driving force of the overall liquid circulation results from the gas hold-up difference between the riser (ε_r) and the downcomer (ε_d), and also from the dispersion height. Gas hold-up is defined as the ratio of volume occupied by the gas phase over the total volume of the corresponding section. Dispersion height (h_D) corresponds to the distance from the surface in which a gas phase can be observed in the riser.

The overall liquid circulation velocity in the riser U_{Lr} can therefore be predicted from an energy balance using Equation 15 (Chisti, 1989):

$$U_{Lr} = \left[\frac{2g \cdot h_D \cdot (\varepsilon_r - \varepsilon_d)}{\frac{K_T}{(1 - \varepsilon_r)^2} + \left(\frac{A_r}{A_d} \right)^2 \frac{K_B}{(1 - \varepsilon_d)}} \right] \quad (15)$$

K_T coefficient taking into account the effects of pressure drop in the riser and the separator section and K_B accounts for pressure drop in the downcomer and the junction.

A_d : cross-sectional area of the downcomer (m^2) and A_r : cross-sectional area of the riser (m^2)

The superficial liquid velocity in the riser (U_{Ld}) is deduced from a mass balance on the liquid phase:

$$U_{Lr} = \frac{A_d}{A_r} U_{Ld} \quad (16)$$

In order to transform this reactor to an electrochemical one, the gas phase is not injected, but electrochemically-generated. This means that both h_D and ε_r depend on the axial position of the electrodes in the riser. At constant current density, ε_r should vary approximately as dispersion height h_D when electrode position is modified, provided $\varepsilon_r \ll 1$. One can deduce from Equations (15) and (16) that $U_{Ld} \sim h_D$.

The objective of complete flotation may be achieved only if hydrodynamic shear forces remain weak in the riser to avoid floc break-up and in the separator to limit break-up and erosion, which means low U_{Ld} values.

3.5.1 Reactor design

An external-loop airlift made of transparent plexiglas is used for this study. The reactor geometry is illustrated by figure 12. By definition, the riser is the section in which the gas phase is sparged and flows upwards. The diameters of the riser and the downcomer are respectively 94mm and 50 mm. Consequently, the riser-to-downcomer cross-sectional ratio (A_r/A_d) is about 3.5. This is a typical value when reaction takes place only in the riser section. Both are 147 cm height ($H_2 + H_3$) and are connected at the bottom by a junction of 50 mm diameter and at the top by a gas separator (also denoted gas disengagement section) of $H_5 = 20$ cm height. The distance between the vertical axes of the riser and the downcomer is 675 mm, which limits the recirculation of bubbles/particles from the riser into the downcomer. At the bottom, the curvature radius of the two elbows is 12.5 cm in order to minimize friction and avoid any dead zone. The liquid volume depends on the clear liquid height (h) and can be varied between 14 L and 20 L, which corresponds to a clear liquid level between 2 cm and 14 cm in the separator section. All the experiments are conducted at room temperature (20 ± 1 °C) and atmospheric pressure in the semi-batch mode (reactor open to the gas, closed to the liquid phase). Contrary to conventional operation in airlift reactors, no gas phase is sparged at the bottom in the riser. Only electrolytic gases induce the overall gas recirculation resulting from the density difference between the fluids in the riser and the downcomer. Two readily available aluminum flat electrodes of rectangular shape (250mm×70mm×1 mm) are used as the anode and the cathode, which corresponds to $S = 175$ cm² electrode surface area (Fig. 12). The distance between electrodes is $e = 20$ mm, which is a typical value in EC cells. They are treated with a HCl aqueous solution for cleaning prior use to avoid passivation. The electrodes are placed in the riser, parallel to the main flow direction to minimize pressure drop in the riser and maximize the recirculation velocity. The axial position of the electrode can also be varied in the column. The distance (H_1) between the bottom of the electrodes and the bottom of the riser ranged between 7 cm and 77 cm. EC is conducted in the intensiostat mode, using a digital DC power supply (Didalab, France) and recording potential during the experiments. The width of the electrodes is maximized by taking into account riser diameter and electrode inter-distance. Current density values (j)

between 5.1 and 51 mA/cm² are investigated, which corresponds to current ($I = jS$) in the range 1.0–10 A.

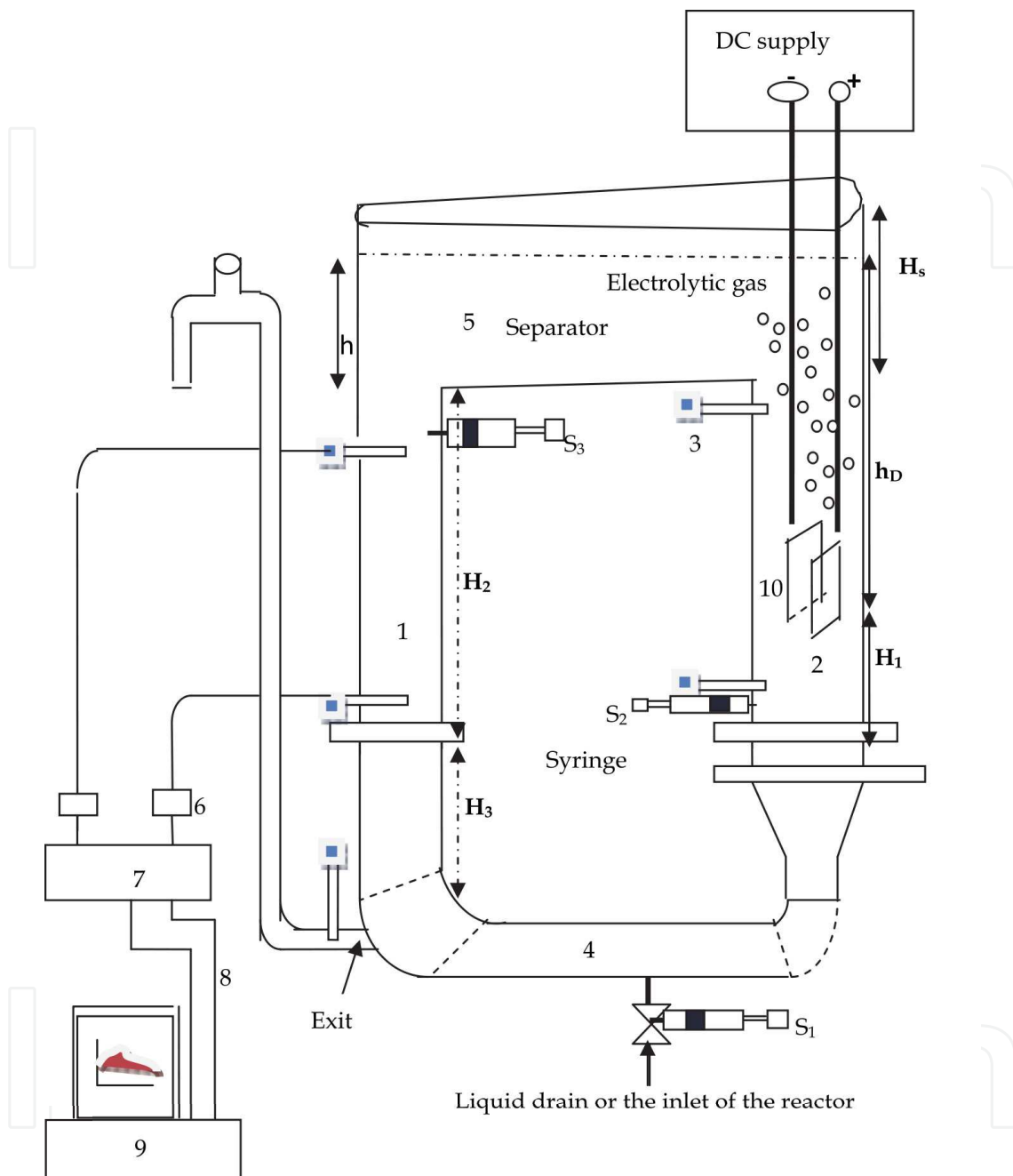


Fig. 12. External-loop airlift reactor (1: downcomer section; 2: riser section; 3: conductivity probes; 4: junction column; 5: separator 6: conductimeter; 7: analog output/input terminal panel (acquisition system); 8: 50-way ribbon cable kit; 9: data acquisition system; 10: electrodes).

3.5.2 Chemicals and methods

The average liquid velocity in the downcomer (U_{Ld}) is measured using the conductivity tracer technique. Two conductivity probes placed in the downcomer section were used to

record the tracer concentration resulting from the injection of 5mL of a saturated NaCl solution at the top of the downcomer using a data acquisition system based on a PC computer equipped with UEI-815 A/D converter. The distance between the probes is 90 cm. Liquid velocity is estimated using the ratio of the mean transit time between the tracer peaks detected successively by the two electrodes and the distance between the probes. The superficial liquid velocity in the riser (U_{Lr}) is deduced from a mass balance on the liquid phase: $U_{Lr} = A_d / A_r U_{Ld}$.

An example of experimental data provided by the conductivity tracer technique is reported in figure 13.

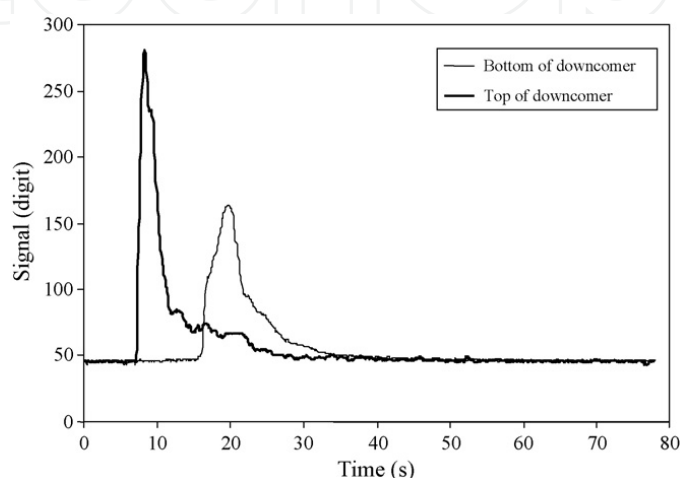


Fig. 13. Example of experimental data from conductivity tracer experiments in the downcomer section when current density $j=21.4 \text{ mA/cm}^2$.

Experiments are carried out using a red dye solution consisting of a mixture of 2-naphthoic acid and 2-naphthol with a total concentration $C_0 = 20 \text{ mg/L}$. Synthetic solutions were prepared by dissolving the dye in tap water. Solution conductivity and pH are measured using a CD810 conductimeter (Radiometer Analytical, France) and a Profil Line pH197i pHmeter (WTW, Germany).

Dye concentration is estimated from its absorbance characteristics in the UV-Vis range at maximum wavelength A_{450} ($\lambda_{max}=450 \text{ nm}$) using a UV-Vis spectrophotometer (Pye Unicam, SP8-400, UK).

The objective of complete flotation may be achieved only if hydrodynamic shear forces remain weak in the riser to avoid floc break-up and in the separator to limit break-up and erosion, which means low U_{Ld} values.

At constant electrode geometry, the solution consists of an adequate selection of U_{Ld} resulting from a compromise between mixing and floc stability. This can be obtained first by optimizing the axial position of the electrodes using both the conductivity tracer technique for U_{Ld} estimation and turbidity measurements to estimate the amount of dispersed Al particles in the downcomer. Experimental results show that no liquid overall circulation can be detected when the electrodes were placed in the upper part of riser, for H_1 approximately higher than 60 cm. For $7 \text{ cm} < H_1 < 60 \text{ cm}$, U_{Ld} decreases when H_1 increases. Overall liquid velocities in the downcomer for two axial positions are reported in figure 14 at various current densities.

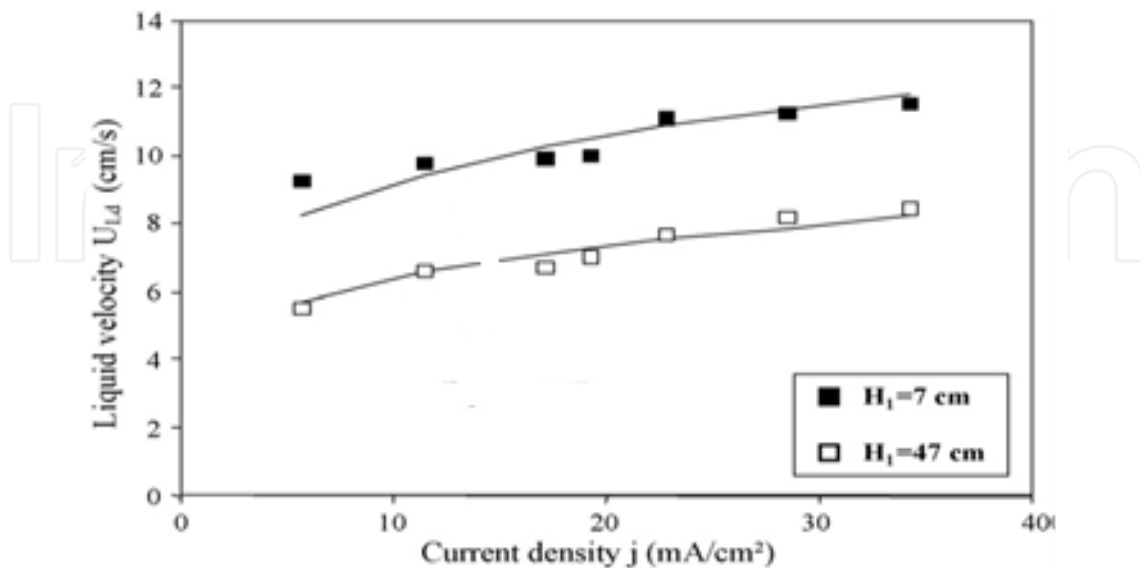


Fig. 14. Influence of the axial position of the electrodes (H_1) and current density (j) on the overall liquid recirculation U_{Ld} ($h=14$ cm; initial pH: 8.3; initial conductivity: $\kappa=2.4$ mS/cm).

Two-parameter model is used to fit the data. The results are given in equation (17):

$$U_{Ld} = 5.8 \cdot \left(\frac{h_D}{h_{Dmax}} \right) \cdot j^{0.20} \quad (\text{cm/s}) \quad (17)$$

in which h_{Dmax} is the maximum dispersion height corresponding to $H_1=7$ cm. This equation confirms the key role of the axial position of the electrodes on reactor hydrodynamics and mixing properties, and the weaker influence of current.

The corresponding turbidity data based on A_{450} without filtration is reported in figure 15 for an electrolysis time of 10 min and two axial positions of the electrodes. In all cases, flocs occupy nearly 1 cm thickness at the free surface of the disengagement section and no settling is reported in the junction and in the separator. Figure 15 shows however that turbidity rose when $H_1 = 7$ cm for current density higher than 15 mA/cm². This corresponds to U_{Ld} values in the range 9–10 cm/s in figure 15. Conversely, complete flotation is always observed for $H_1 = 47$ cm, as A_{450} remains low, about 0.06. As a result, electrode position must be chosen in order to maintain U_{Ld} always lower than 9 cm/s, regardless of current density in the range of j studied (Fig. 15). Such a condition is achieved for $H_1 = 47$ cm, as shown in figure 15, which corresponds nearly to mid-height in the riser. However, $H_1 = 47$ cm is only a coarse approximation of the optimum electrode height, but the simple way to optimize mixing conditions does not consist in adjusting precisely H_1 because it is easier from a practical point of view to adjust the clear liquid height h . Indeed, h affects simultaneously h_D and h_{Dmax} in Eq. (17), but its range ($2 \text{ cm} < h < 14 \text{ cm}$ in this work) is usually far smaller than H_1 (between 7 and 77 cm).

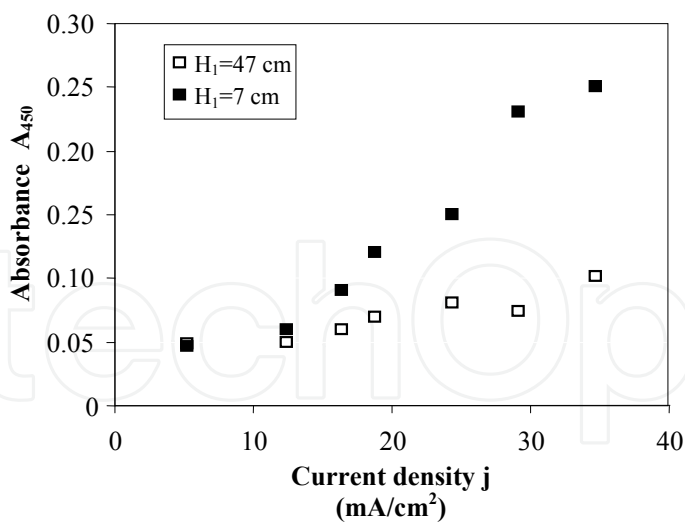


Fig. 15. Evolution of absorbance A_{450} of non-filtered samples after 10 min operation with 1 cm of floc thickness already formed as a function of superficial liquid velocity U_{ld} in the downcomer (initial pH: 8.3, conductivity: $\kappa=2.4$ mS/cm).

3.5.3 Some results

The efficiency of electrocoagulation/electroflotation in removing colour from synthetic textile wastewater by using aluminum and iron electrodes in an external-loop airlift reactor is presented. Disperse, reactive and the mixture are used to determine the optimized parameters.

The real textile wastewater is then used using the optimized parameters. Three effluents were also used: disperse, reactive and the mixture. Energy is determined for each kind of dye.

3.5.3.1 Synthetic dye

For this synthetic dye, chemical oxygen demand (COD) is measured using the standard closed reflux colorimetric method. Initial COD was about 2500 mg O₂/L. Initial pH is varied between 5 and 10 using minute addition of 0.1 M H₂SO₄ or NaOH solutions. The conductivity κ (i.e. the ionic strength) of dye solutions is adjusted by sodium chloride addition in the range 1.0–29 mS/cm, which covers the range usually explored in the literature.

COD, color removal and turbidity efficiencies (Y_{COD} , Y_{COL} and Y_{ABS}) are expressed as percentage and defined as:

$$Y_{COD} = \frac{COD(t = 0) - COD(t)}{COD(t = 0)} \tag{18a}$$

$$Y_{COL} = \frac{A_{450}(t = 0) - A_{450}(t)}{A_{450}(t = 0)} \tag{18b}$$

Y_{COL} and Y_{ABS} are obtained using the same equation (Eq.18b), but Y_{COL} was based on absorbance measurements at 450 nm after filtration, while Y_{ABS} is measured without

filtration/decantation. Y_{ABS} is used to analyze qualitatively the evolution of turbidity over time. This parameter shows whether the flocs float or are destroyed and driven by the liquid flow. The influence of the initial pH on COD and turbidity removals is illustrated in Figure 16 at constant current density and initial conductivity. An optimum is found for the initial pH, which is between 7.0 and 8.0, although it differs slightly between COD and color removal yields.

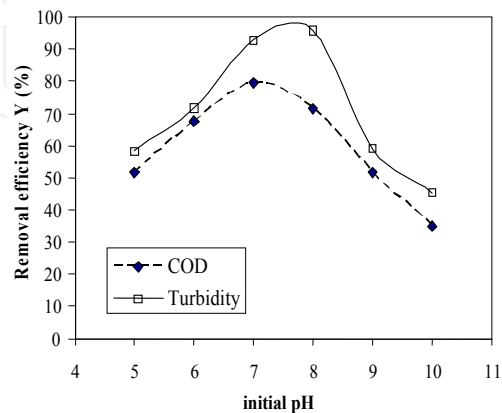


Fig. 16. Influence of the initial pH on COD removal and decolorization after 8 minutes operation (conductivity: $\kappa=2.4$ mS/cm, current density: $j=28.5$ mA/cm²).

The influence of conductivity is illustrated in Figure 17 shows an increase of Y_{COD} and Y_{COL} with κ for the red dye between 2 and 28 mS/cm. Y_{COL} enhancement becomes however slight when κ is higher than 15 mS/cm.

The decrease in specific energy consumption E_{dye} due to the increase of conductivity is illustrated by Figure 18. This figure indicates that E_{dye} can be divided roughly by a factor 13 when conductivity is multiplied by a factor 12.

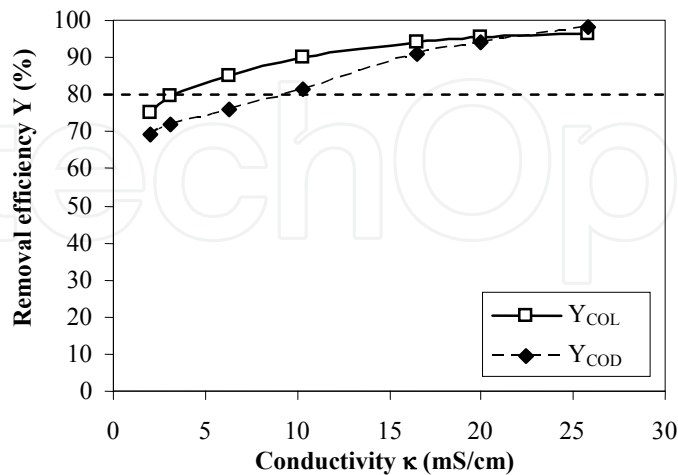


Fig. 17. Influence of conductivity κ on COD and color removal efficiencies (initial pH: 8.3; current density: $j=28.6$ mS/cm).

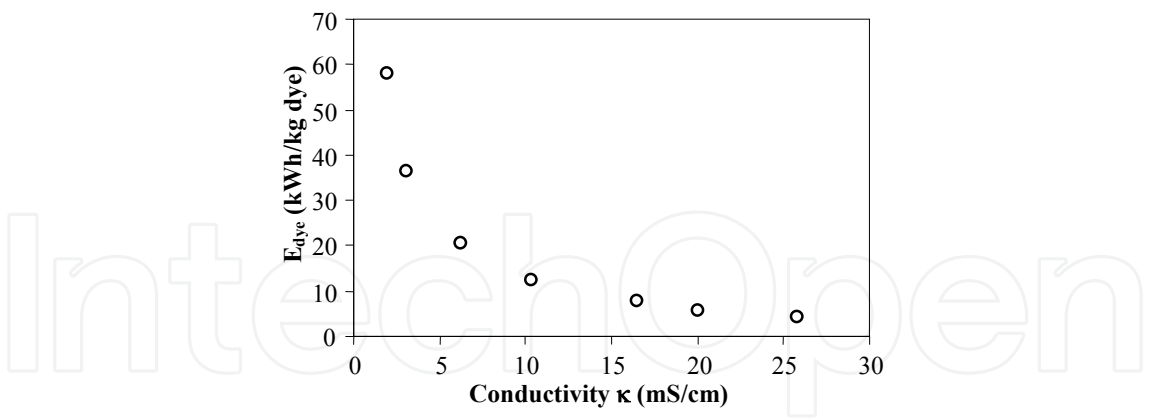


Fig. 18. Influence of conductivity κ on energy consumption E_{dye} at constant current density j and operation time (initial pH: 8.3).

3.5.3.2 Real textile dye

The real textile wastewater is then used. Three effluents are also used: disperse, reactive and the mixture. The color efficiency is between 70 and 90% and COD efficiency reached 78%. The specific electrical energy consumption per kg dye removed (E_{dye}) in optimal conditions for real effluent is calculated. 170 kWh/kg dye is required for a reactive dye, 120 kWh/kg dye for disperse and 50 kWh/kg dye for the mixture.

For disperse dye, the removal efficiency is better using aluminium electrodes, whereas, the iron electrodes show more efficiency for removing colour for reactive dye and mixed synthetic dye.

Figure 19 shows a photo representing a real effluent before EC treatment and 10 minutes after EC treatment.

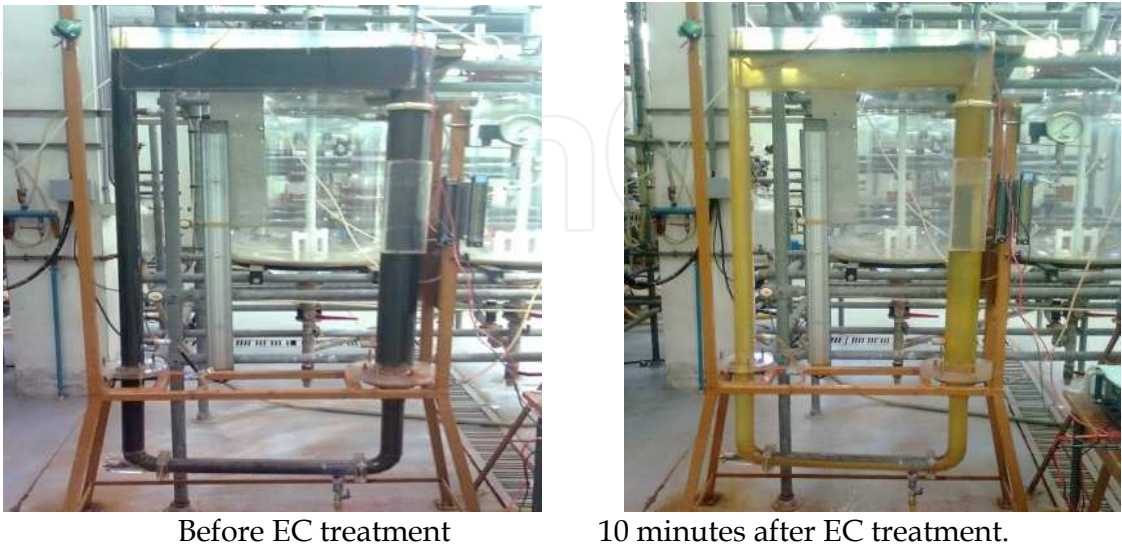


Fig. 19. Photo showing decolourization by EC in external loop airlift reactor of real textile dye.

3.5.3.3 Defluoridation of drinking water

An excess amount of fluoride anions in drinking water has been known to cause adverse effects on human health. To prevent these harmful consequences, especially problems resulting from fluorosis, the World Health Organization (WHO) fixed the maximum acceptable concentration of fluoride anions in drinking water to 1.5 mg/L (Essadki et al., 2009).

The defluoridation of drinking water by EC is studied in the same reactor. Current density values j between 2.8 and 17 mA/cm² are investigated, which corresponded to current ($I=j \cdot S$) in the range 0.5–3 A. Samples are filtered and the concentrations of the remaining fluoride content are determined in the solution by means of a combined selective fluoride electrode ISEC301F and a PhM240 ion-meter (Radiometer Analytical, France), using the addition of a TISAB II buffer solution to prevent interference from other ions.

Experiments are carried using an initial fluoride concentration $[F^-]_0$ between 10-20 mg/L by adding sodium fluoride NaF (Carlo Erba Réactifs, France). The efficiency of fluoride removal can be calculated as follows:

$$Y(\%) = 100 \times \frac{[F^-]_0 - [F^-]}{[F^-]_0}$$

(19)

$[F^-]_0$: the initial fluoride concentration .
 $[F^-]$: the remaining concentration of fluoride .

Figure 20 shows the effect of the current intensity on the evolution of the fluoride concentration. For $I = 0.5A$ corresponding to a current density of 2.85mA/cm², fluoride concentration reaches only 4.5 mg/L for an electrolysis time of 30 min. Conversely, for exceeding 1A, i.e. for a current density higher than 5.7mA/cm², one converges towards a concentration of 1mg/L and more rapidly as current density is increased. This confirms that defluoridation can be achieved at low current density. The relatively low efficiency observed at 0.5A can be attributed to the weak charge loading produced in this case, 0.47 F/m³. As expected, the efficiency of EC depends on the amount of coagulant produced in situ.

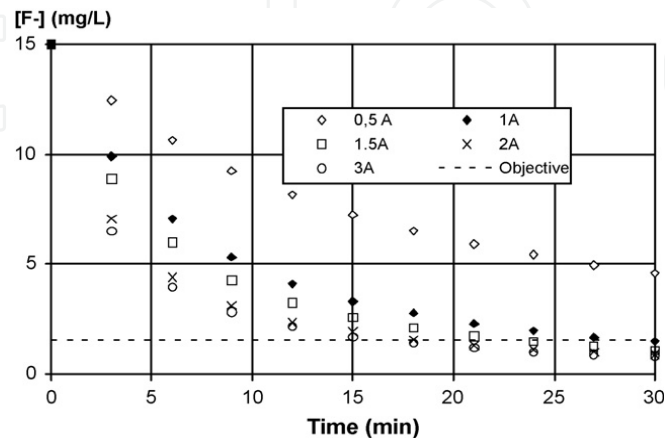


Fig. 20. Evolution of fluoride concentration during EC in the STR: influence of current intensity (initial pH 7.4 and $C_0 = 15\text{mg/L}$).

3.5.4 External loop airlift reactor as a continuous reactor

The reactor is operated in a continuous flow of liquid. The inlet volumetric liquid flow-rate Q_L varied between 0.1 and 2 L/min.

A study of the residence time distribution (RTD) analysis of liquid phase has been performed. The liquid RTD is determined by means of the tracer response technique. An approximated δ -Dirac pulse of tracer solution (NaCl) is injected into the reactors at a certain time ($t = 0$) and the outlet signal is detected by conductivity probe and recorded by the acquisition system. The tracer is injected as quickly as possible to obtain as closely as practical a δ -pulse of tracer at the inlet.

The syringe (S_1) was introduced in the drain that is open to the flow and representing the inlet of the whole reactor. The probe conductivity is placed at the exit position of the reactor (Fig.12). Examples of RTD measurements are shown in figure 21. Two kinds of signal are observed in this figure. One showed two peaks for the case of $Q_L = 0.36$ L/min, $I = 6$ A, $H_1 = 7$ cm and the other showed one peak for the case of $Q_L = 0.73$ L/min, $I = 1$ A, $H_1 = 47$ cm.

The main flow (Q_L) is divided into two flows: one exit directly the reactor by crossing the junction and the other crosses the riser, the separator zone and the downcomer to exit. The percentage of flow that quit the reactor without reacting increased when the main flow increased and the current intensity decreased. The experiments confirm also that the liquid crosses the reactor without achieving loops in the case of the continuous flow.

So to support the reaction during the electrocoagulation, it is necessary to amplify the current intensity and to decrease the inlet flow.

Interesting results are also obtained:

- The superficial liquid velocity (U_{Ld}) at the downcomer, decreases when the volume inlet flow increases ($0 < Q_L < 2$ L/min).

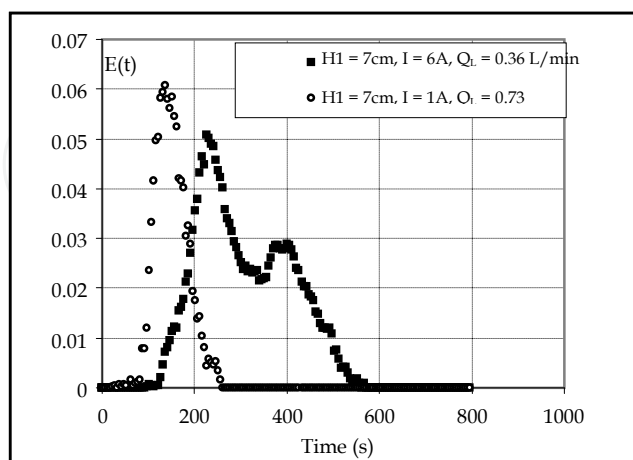


Fig. 21. E-curve as a global RTD in External-loop airlift reactor for ($Q_L = 0.36$ L/min, $I = 6$ A, $H_1 = 7$ cm: 2 peaks) and ($Q_L = 0.73$ L/min, $H_1 = 7$ cm, $I = 1$ A, 47 cm: 1 peak).

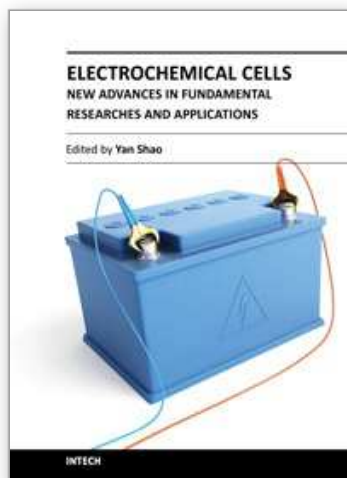
4. Conclusion

External-loop airlift reactors have been shown to be versatile tools to carry out EC with complete flotation, using only electrochemically generated H_2 bubbles to achieve an overall liquid circulation and good mixing conditions. Consequently, the use of mechanical agitation, pumping or compressed air was not necessary. This could not be achieved in other kinds of conventional gas-liquid contacting devices than airlift reactors. External-loop devices are particularly adapted because they offer specific designs for the disengagement section that allow large distance between riser and downcomer. This improves flotation by minimizing the recirculation of aluminum or iron particles in the downcomer. These results were obtained by the adequate selection of the axial position of the electrodes (H_I) and the liquid height in the separator section (h) in order to avoid floc break-up in the riser and floc erosion at the free surface. A limiting value of the liquid velocity in the downcomer was defined, while U_{Ld} was correlated to dispersion height h_D and current density j (Equation 17). These can be used at constant j and A_r/A_d ratio for scale-up purpose.

To increase the efficiency of EC in a continuous reactor, the mean residence time should be increased. The experiments showed that this effect is reached in the case of a relatively high value of current density and weak value of the inlet flow-rate. This study highlighted the hydrodynamic aspect of the flow in the external airlift reactor functioning as a batch and continuous reactor. The design of this kind of reactor should be improved to allow the reactant to follow the compartment in which the reaction takes place (riser).

5. References

- Chen G., (2004), *Sep. Purif. Technol.* 38, 11–41.
- Chisti Y., (1989), *Airlift Bioreactors*, Elsevier, London.
- Essadki H., Nikov I., Delmas H., (1997), *Electrochemical Probe for Bubble Size Prediction in a Bubble Column*, *Experimental Thermal and Fluid Science*, 243-250.
- Essadki A.H., Gourich B., Vial Ch., Delmas H., Bennajah M., (2009), *Defluoridation of drinking water by electrocoagulation/electroflotation in a stirred reactor with a comparative performance to an external-loop airlift reactor*, *Journal of Hazardous Materials* 168, 1325-133.
- Levart E., and Schumann D., (1974), *Analyse du Transport Transitoire sur un Disque Tournant en Régime Hydrodynamique Laminaire et Permanent*, *Int. J. Heat Mass Transfer* 17, 555–566.
- L.P.Reiss and T.I.Hanratty , *An experimental study of the unsteady nature of the viscous sublayer*, *AIChE J*, 9, (1963), 154-160.



Electrochemical Cells - New Advances in Fundamental Researches and Applications

Edited by Dr. Yan Shao

ISBN 978-953-51-0032-4

Hard cover, 240 pages

Publisher InTech

Published online 07, March, 2012

Published in print edition March, 2012

Currently the research field of electrochemical cells is a hotspot for scientists and engineers working in advanced frontlines of micro-, nano- and bio-technologies, especially for improving our systems of energy generation and conversation, health care, and environmental protection. With the efforts from the authors and readers, the theoretical and practical development will continue to be advanced and expanded.

How to reference

In order to correctly reference this scholarly work, feel free to copy and paste the following:

Abdel Hafid Essadki (2012). Electrochemical Probe for Frictional Force and Bubble Measurements in Gas-Liquid-Solid Contactors and Innovative Electrochemical Reactors for Electrocoagulation/Electroflotation, *Electrochemical Cells - New Advances in Fundamental Researches and Applications*, Dr. Yan Shao (Ed.), ISBN: 978-953-51-0032-4, InTech, Available from: <http://www.intechopen.com/books/electrochemical-cells-new-advances-in-fundamental-researches-and-applications/electrochemical-probe-for-frictional-force-and-bubble-measurements-in-gas-liquid-solid-contactors-an>

INTECH
open science | open minds

InTech Europe

University Campus STeP Ri
Slavka Krautzeka 83/A
51000 Rijeka, Croatia
Phone: +385 (51) 770 447
Fax: +385 (51) 686 166
www.intechopen.com

InTech China

Unit 405, Office Block, Hotel Equatorial Shanghai
No.65, Yan An Road (West), Shanghai, 200040, China
中国上海市延安西路65号上海国际贵都大饭店办公楼405单元
Phone: +86-21-62489820
Fax: +86-21-62489821

© 2012 The Author(s). Licensee IntechOpen. This is an open access article distributed under the terms of the [Creative Commons Attribution 3.0 License](#), which permits unrestricted use, distribution, and reproduction in any medium, provided the original work is properly cited.

IntechOpen

IntechOpen